Electronic Supplementary Information

# Mechanical-dielectric optimized graphene aerogels with strain-tunable microwave attenuation and shielding functions

Yijing Zhao [a], Nasir Ahmad [a], Yong Yang [b, *], Wei Zhai [a, *]

[a] Department of Mechanical Engineering, National University of Singapore, 9 Engineering Drive 1, 117575, Singapore. E-mail: mpezwei@nus.edu.sg

[b] National University of Singapore, 5A Engineering Drive 1, 117411 Singapore. E-mail: tslyayo@nus.edu.sg

## SectionS1. Experimental methods

### 1.1 Materials

Silicon carbide (SiC) nanowires with a diameter range from 50-500 nm and length range from 50-100 μm were sourced from Changsha Sinet Advanced Materials Co. Ltd., Carboxylated multi-walled carbon nanotubes (CNTs) were supplied by XF NANO Co. Ltd., China. Graphene oxide (GO) suspensions were obtained from Graphenea Inc.

### 1.2 Preparation of SCGAs

A series of SCGAs were prepared through a bidirectional freeze casting and thermal reduction process. Initially, CNTs were added to GO solutions (4 mg/ml) at a CNT/GO mass ratio of 3:2 and ultrasonicated for 1 h to form a homogeneous CNT/GO suspension. Subsequently, different amounts of SiC nanowires were added to the CNT/GO suspension, followed by 2 h of ultrasonication for uniform dispersion, and the mixture was stirred continuously for freeze casting. The bidirectional freeze casting of the mixed SiC NW/CNT/GO suspension was conducted by transferring the suspension into homemade Teflon molds and freezing it at -60 °C. The Teflon molds are equipped with bidirectional copper plates and PDMS insulators to realize the dual-direction temperature gradient within the suspension. After complete freezing, the samples were freeze-dried for 72 h to obtain SiC NW/CNT/GO aerogels and subsequently underwent high-temperature thermal reduction at 800 °C under an Ar atmosphere for 1 h to obtain SiC NW/CNT/Graphene aerogels (SCGAs). According to the mass ratio of SiC NW:CNT:GO in the prepared suspension, which is 2:3:2, 4:3:2, and 6:3:2, the obtained aerogels are named SCGA-1, SCGA-2, and SCGA-3, respectively. For comparison, CNT/graphene aerogels (CGAs) without SiC nanowires, alongside pristine graphene aerogels (GAs) are prepared using the same procedure.

## SectionS2. Characterization, measurements, calculation, and simulation

### 2.1 Morphology, phase structure, mechanical and thermal properties

The microstructure and elemental composition of aerogels were investigated utilizing a Hitachi S-4300 field emission scanning electron microscope (FE-SEM). The Zeta potential of the mixed solution was measured using a Malvern Zetasizer Nano ZS90, while the viscosity was determined with a LICHEN NDJ digital viscometer. The crystallographic structures were determined by X-ray diffraction (XRD) using a Shimadzu diffractometer equipped with Cu Kα radiation (λ = 0.15418 nm). Raman spectral analysis was performed using a Renishaw In-Via spectrometer equipped with a 514 nm laser. Mechanical compression testing was performed on an Instron 5848 micro-tester at a constant velocity of 5 mm/min for both compression and release. Electrical conductivity (σ) was determined based on the formula $\sigma = t/(R \times A)$, where t represents sample thickness, R is the resistance measured, and A the electrode area. Additionally, thermal imaging was executed using a FLIR T1020 HD camera to assess thermal properties. The contact angle of the aerogels was measured using a Contact Angle Machine SDC-80 (SINDIN). Environmental humidity was recorded using a hygrometer (testo 608-H1).

### 2.2 Microwave attenuation measurements

To measure the electromagnetic parameters of the aerogel across the 2-18 GHz broadband range, the coaxial line method was employed to determine the permittivity for microwave attenuation calculations. The toroidal specimens were prepared by infiltrating the aerogel with wax and molding it into a coaxial ring, with external and internal diameters of 7 mm and 3 mm, respectively, and a thickness of 2 mm. The

process of infusing aerogel with paraffin wax involves the following steps: First, the aerogels are immersed in molten paraffin wax. The samples are then allowed to sit undisturbed for 3 minutes. Next, the aerogels, still submerged in molten wax, are placed in a vacuum oven for continuous impregnation at 120°C for 3 hours. Finally, the wax-infused aerogels are removed and cooled at room temperature to allow the paraffin wax to solidify. The Agilent HP8722D vector network analyzer was employed to test the complex permittivity ($\varepsilon_r = \varepsilon' - j\varepsilon''$) and permeability ($\mu_r = \mu' - j\mu''$) across the 2-18 GHz spectrum. Reflection loss (RL) calculations were performed adhering to transmission-line theory and utilizing the metal back-panel model.

$$Z_{in} = Z_0\sqrt{|\mu_r/\varepsilon_r|}\tanh\left[ j(2\pi fd/c)\sqrt{\mu_r\varepsilon_r} \right] \quad (1)$$

$$RL = 20\log_{10}\left|\frac{Z_{in} - Z_0}{Z_{in} + Z_0}\right| \quad (2)$$

Here, $\varepsilon_r$ and $\mu_r$ represent the complex permittivity and permeability, respectively, while $Z_0$ and $Z_{in}$ indicate the impedance of free space and normalized input impedance, respectively. The variables d, f, and c refer to the thickness of the material being tested, the frequency of the microwaves, and the speed of microwaves in free space, respectively. It is noted that for non-magnetic materials, $\mu_r$ is consistently equal to 1.

In accordance with Debye relaxation theory, Cole-Cole plots are instrumental in delineating the relationship between energy dissipation ($\varepsilon''$) and energy storage capacity ($\varepsilon'$).

$$(\varepsilon' - (\varepsilon_s + \varepsilon_\infty)/2)^2 + (\varepsilon'')^2 = ((\varepsilon_s - \varepsilon_\infty)/2)^2 \quad (3)$$

Here, $\varepsilon_s$ signifies the static permittivity, and $\varepsilon_\infty$ represents the relative dielectric permittivity at an upper frequency limit.

The α value of all the samples is calculated by the following equation.

$$\alpha = \frac{\sqrt{2}\pi f}{c} \times \sqrt{(\mu''\varepsilon'' - \mu'\varepsilon') + \sqrt{(\mu''\varepsilon'' - \mu'\varepsilon')^2 + (\mu''\varepsilon'' + \mu'\varepsilon')^2}} \quad (4)$$

Where c is the light speed in a vacuum. μ' and μ'' are equal to 1 and 0, respectively for non-magnetic materials.

### 2.3 Microwave shielding measurements

The microwave shielding performance was calculated using S-parameters based on the specific sample thickness. Given that the shielding samples have a thickness of 8 mm, which makes it challenging to fabricate coaxial samples for broadband testing, the evaluation of microwave shielding was conducted using a VNA HP8722D in the X-band range from 8.2 to 12.4 GHz, employing a waveguide setup with the sample size of 22.8 mm × 10.16 mm × 8 mm. Key electromagnetic properties such as scattering parameters (S11 and S21), complex permeability, and permittivity were quantified. The coefficients of reflectivity (R, $R = |S11|^2$), transmission (T, $T = |S21|^2$), and absorption (A) were determined to fulfill the relationship A + R + T = 1. Calculations were performed to determine the shielding effectiveness, encompassing total ($SE_{tol}$), reflection ($SE_r$), and absorption ($SE_a$) shielding effectiveness by the following equations:

$$SE_r = -10 \log(1-R) \quad (5)$$

$$SE_a = -10 \log(T/(1-R)) \quad (6)$$

$$SE_{tol} = -10 \log(T) \quad (7)$$

### 2.4 Simulation

Radar Cross Section (RCS) simulations for actual far-field responses at 10 GHz were performed using the High-Frequency Structure Simulator (HFSS, Ansys), with the plane wave incident perpendicular to the sample. The sample model size was set to 200 × 200 × 3 $mm^3$ with a perfect electric conductor (PEC) plate (1mm thick) on the

back. The S21 value and electric field simulation for air, SCGAs under different compression strains, and gradient low-reflection aerogel were conducted by establishing a 20 × 20 × 8 $mm^3$ model without the PEC back in free space. The models were applied with master-slave boundary surfaces to create a periodic array of the model for simulating the infinite plane size. The S21 values were obtained across the X-band, and the electric fields were recorded at 10 GHz. For all the models used in the simulation, their material properties were defined by their tested electromagnetic parameters as a function of frequency.

**SectionS3. Harsh condition treatment**

The harsh condition treatments included heat treatment, combustion, freezing, ultra-low temperature exposure, water droplet testing, and humidity exposure. The heat treatment was conducted by placing SCGAs in an oven at 300°C for 3 hours. For the combustion test, the aerogels were saturated with alcohol and ignited until the alcohol was fully consumed, and the flames extinguished. The freezing treatment involved placing the aerogels on a cooling platform at -80°C for 1 hour. The ultra-low temperature treatment was performed by fully immersing the aerogels in liquid nitrogen for 10 minutes. The water droplet test simulated natural rain conditions by continuously dripping 30 ml of water onto the aerogel surface using a syringe until the entire volume was dispensed. To simulate natural humidity, the aerogels were placed outdoors for a full day and night. On the test day, 28th October 2024, the measured humidity was 85.8%, while the average humidity in Singapore for October 2024 was 83%. These treatments effectively replicate the extreme conditions the materials are likely to encounter in real-world applications.

## SectionS4. Morphology and properties of SCGAs

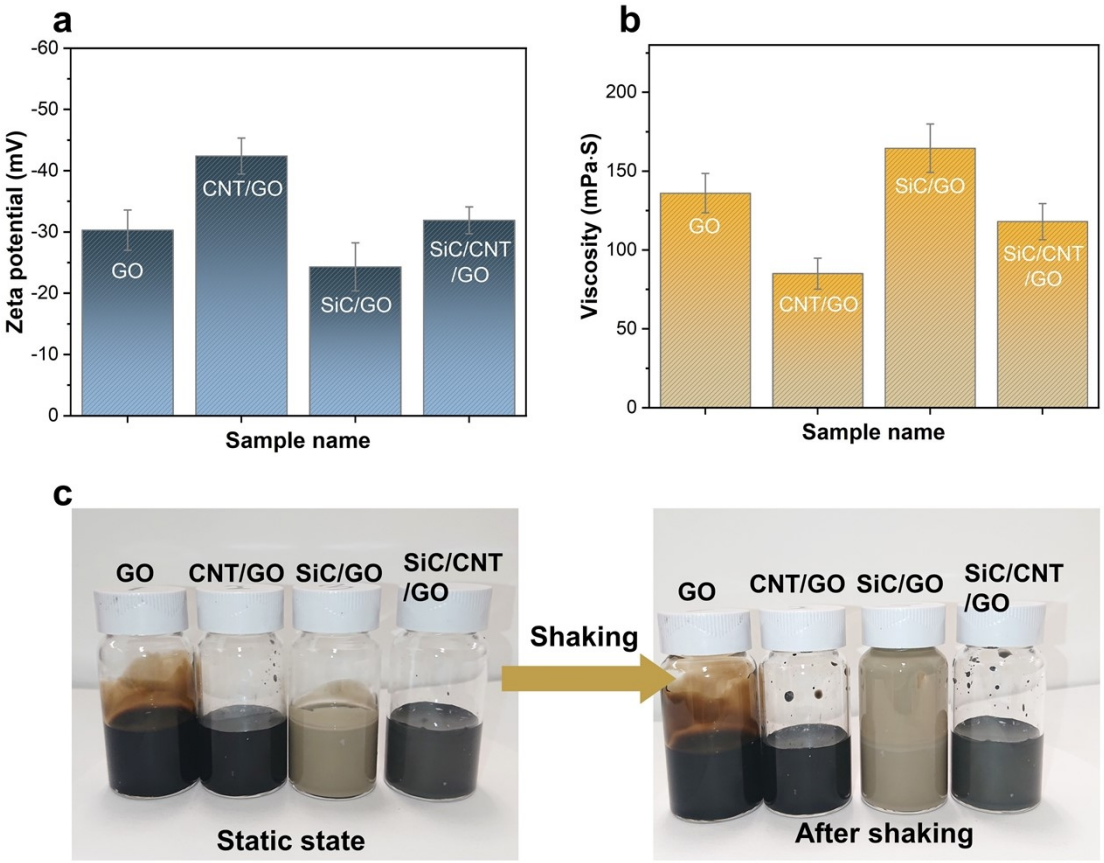


**Fig. S1** (a) Zeta potential, (b) Viscosity, and (c) Digital photos before and after shaking of GO, CNT/GO (3:2), SiC/GO (2:1), and SiC/CNT/GO (4:3:2) suspensions.

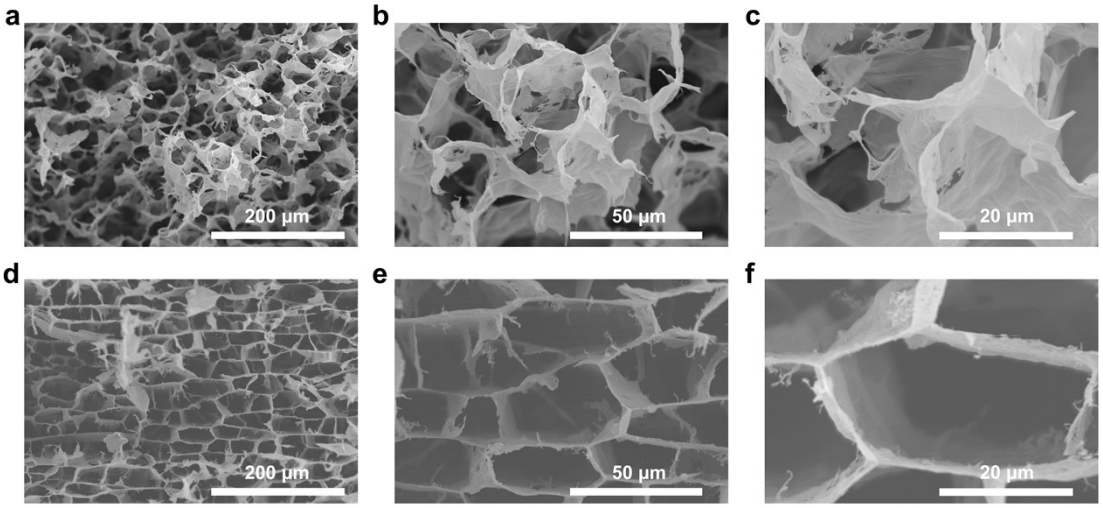


**Fig. S2** SEM images of the (a-c) GAs, and (d-f) CGAs.

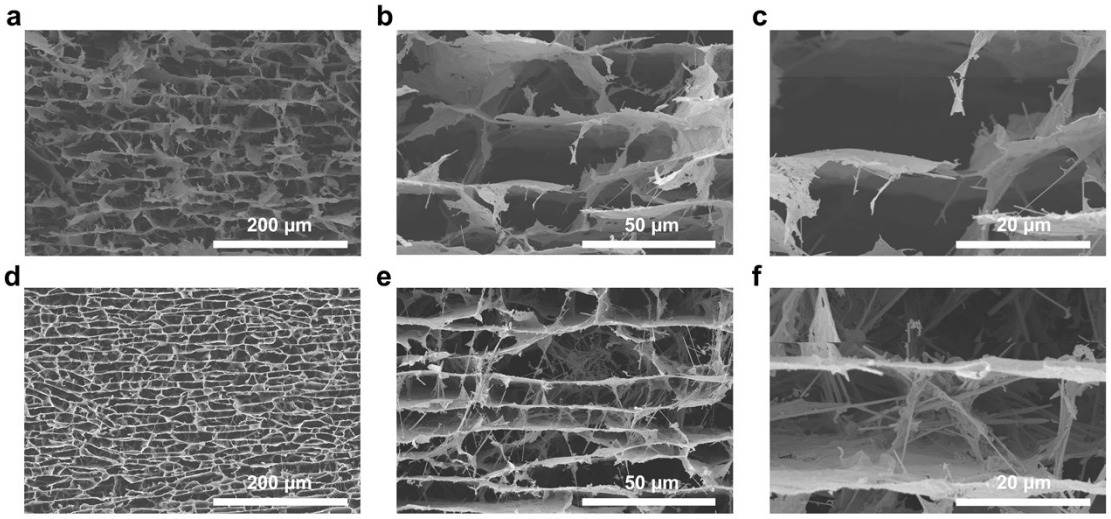


**Fig. S3** SEM images of (a-c) SCGA-1 and (d-f) SCGA-3.

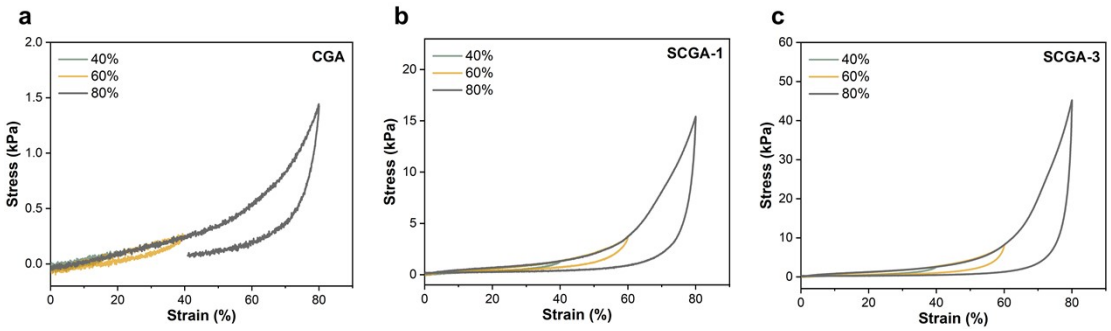


**Fig. S4** Compressive stress-strain (σ-ε) curves of (a) CGA, (b) SCGA-1, and (c) SCGA-3 at 40%, 60% and 80% strain.

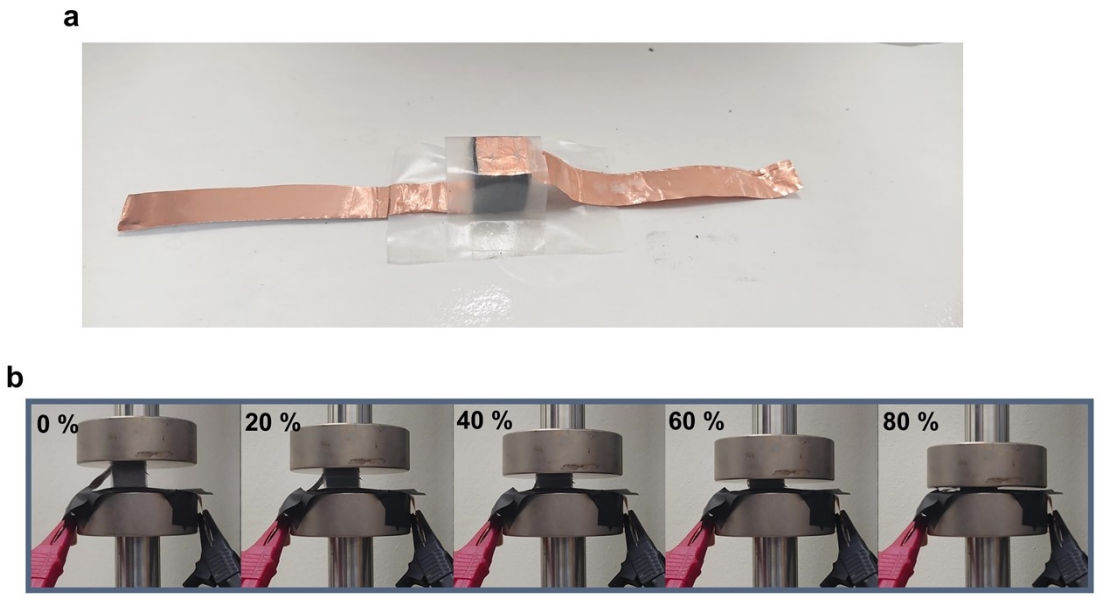


**Fig. S5 (a)** Photograph of the assembled aerogel for real-time resistance test and conductivity calculation. (b) Photograph of the real-time relative resistance change recording of the aerogel

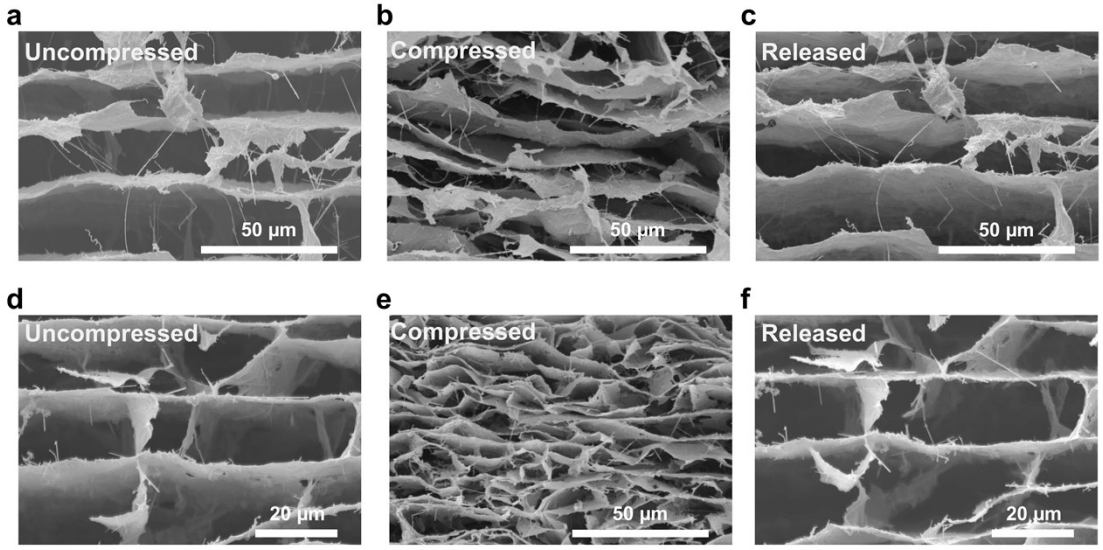


**Fig. S6** SEM images of the SCGA-2 before, under, and after compression under 40% strain (a-c), and 80% strain 2 (d-e).

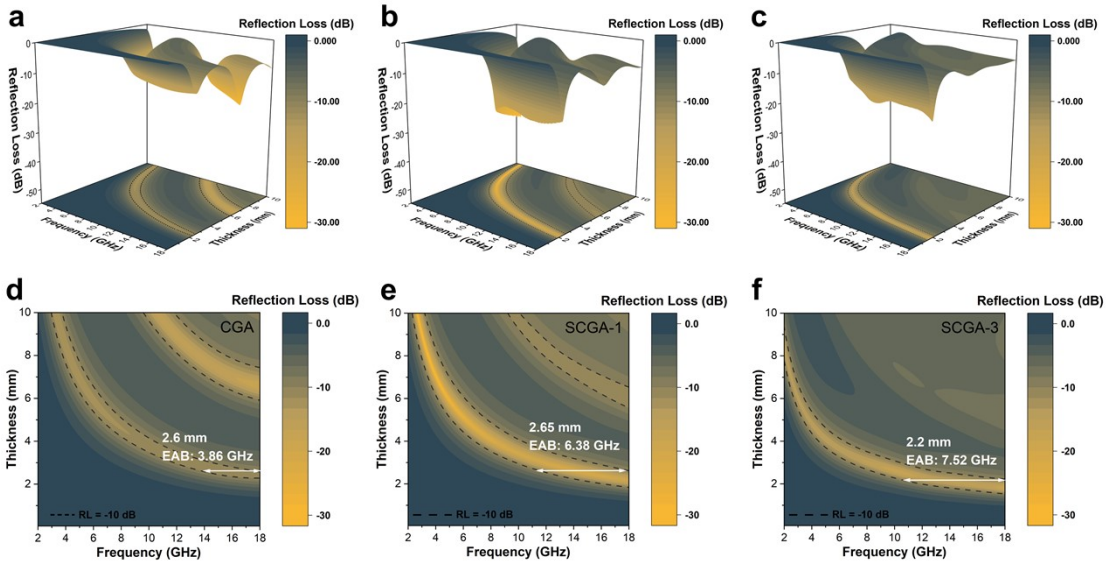


**Fig. S7** The 3D plots of RL values versus frequency and thickness of (a) CGA, (b) SCGA-1, and (c) SCGA-3. The 2D contours of RL values versus frequency and thickness of (d) CGA, (e) SCGA-1, and (f) SCGA-3.

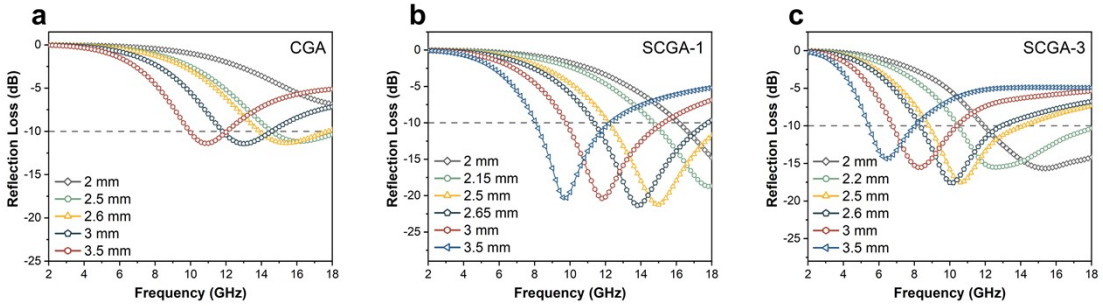


**Fig. S8** 2D plots of RL values versus frequency and specific thickness for sample (a) CGA, (b) SCGA-1, and (c) SCGA-3.

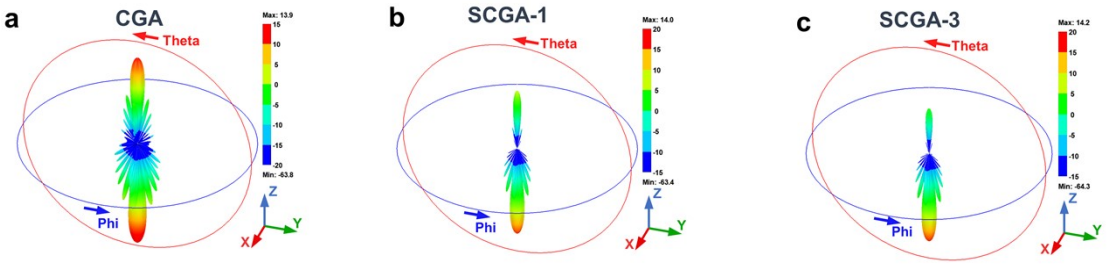


**Fig. S9** 3D RCS simulation chart of PEC back plate covered with (a) CGA, (b) SCGA-1, and (c) SCGA-3, respectively.

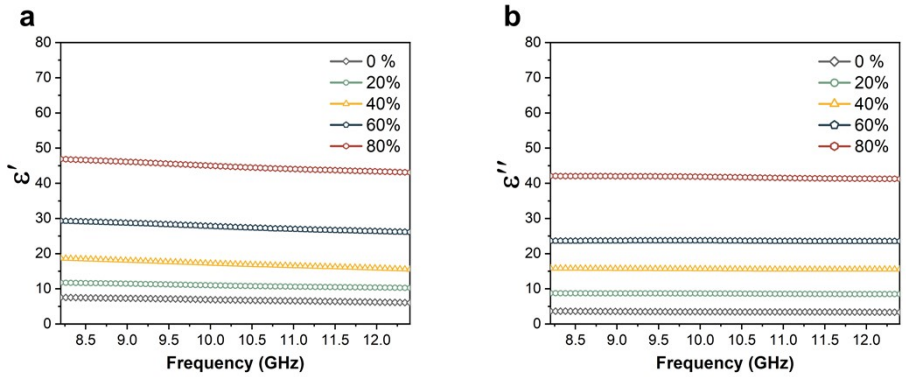


**Fig. S10** The frequency-dependent electromagnetic parameters including (a) ε′ (b) ε″ of sample SCGA-2 under 0%, 20%, 40%, 60%, and 80% compression strain.

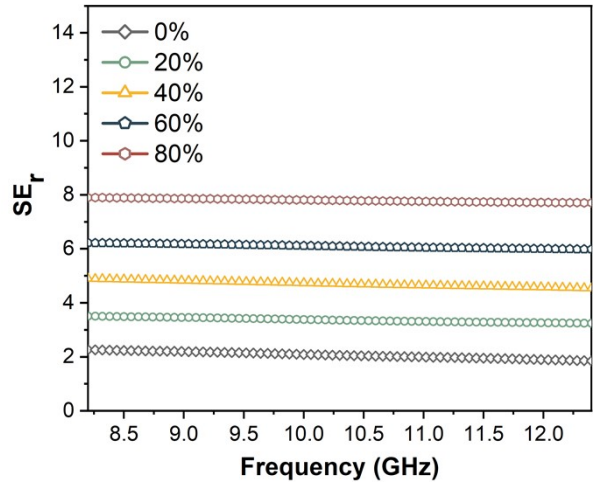


**Fig. S11** The reflection shielding effectiveness ($SE_r$) of sample SCGA-2 under 0%, 20%, 40%, 60%, and 80% compression strain.

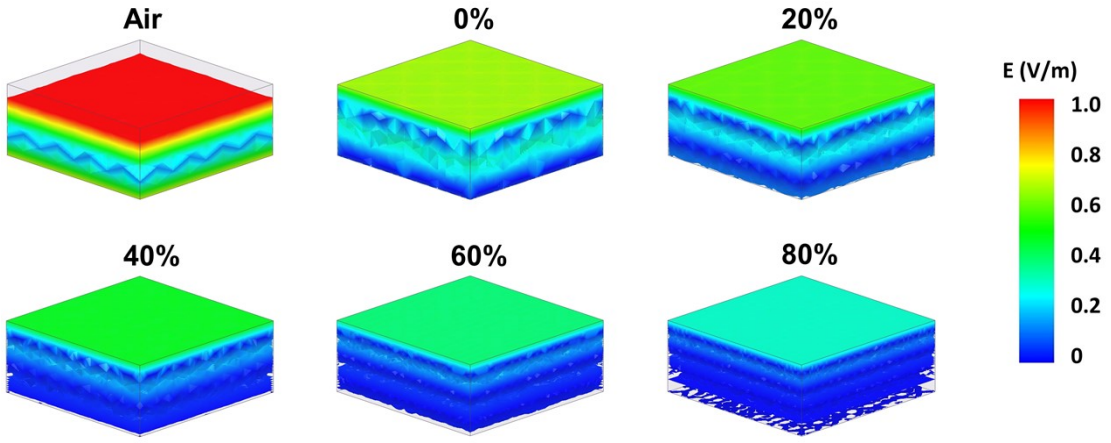


**Fig. S12** 3D simulated electric field intensity of air and sample SCGA-2 under different compression strains when interact with microwaves.

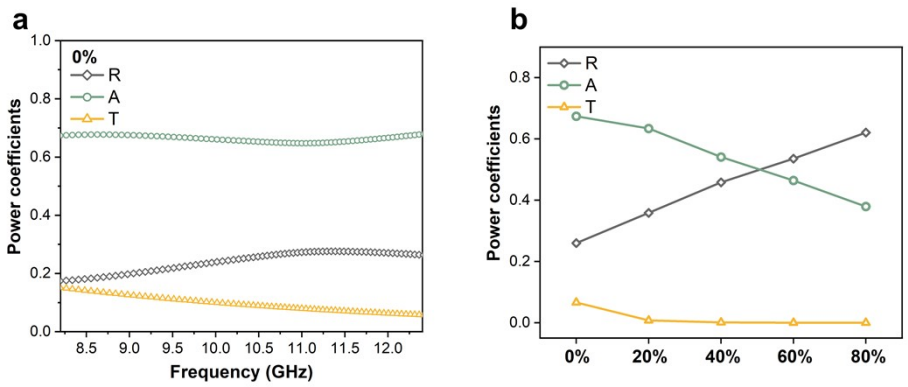


**Fig. S13** (a) Power coefficients of SCGA-2 without compression strain. ((b)The average power coefficients of sample SCGA-2 are under 0%, 20%, 40%, 60%, and 80% compression strain.

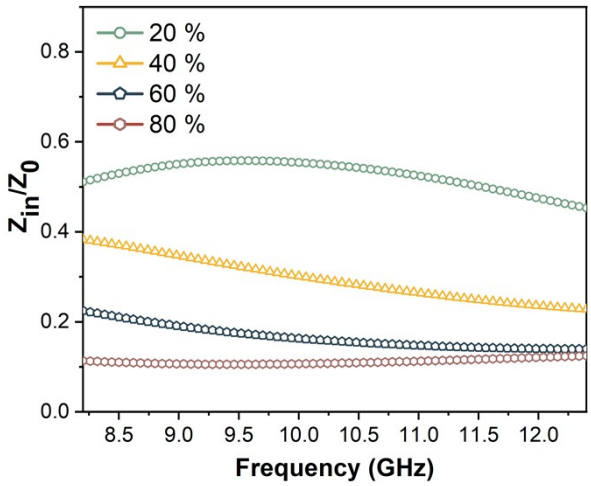


**Fig. S14** The impedance matching ratio $Z_{in}/Z_0$ of sample SCGA-2 under 20%, 40%, 60%, and 80% compression strain at the thickness of 2 mm.

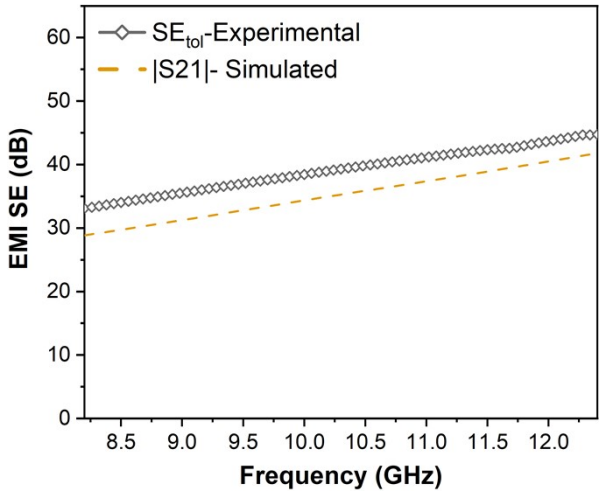


**Fig. S15** The comparison of simulated |S21| and tested $SE_{tol}$ of the gradient low-reflection model.

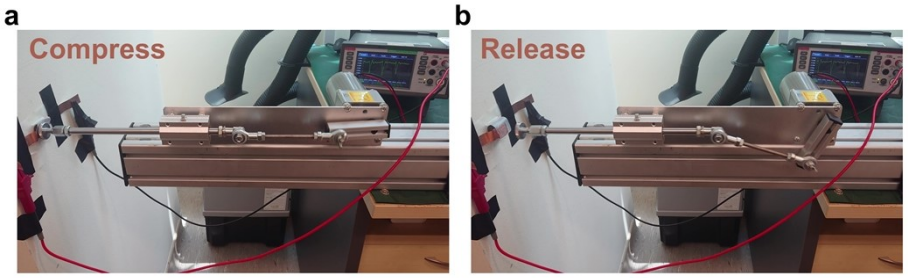


**Fig. S16** Photograph of the setup used to monitor the real-time relative resistance change ($\Delta R/R_0$) of the aerogel during long-term cyclic compression.

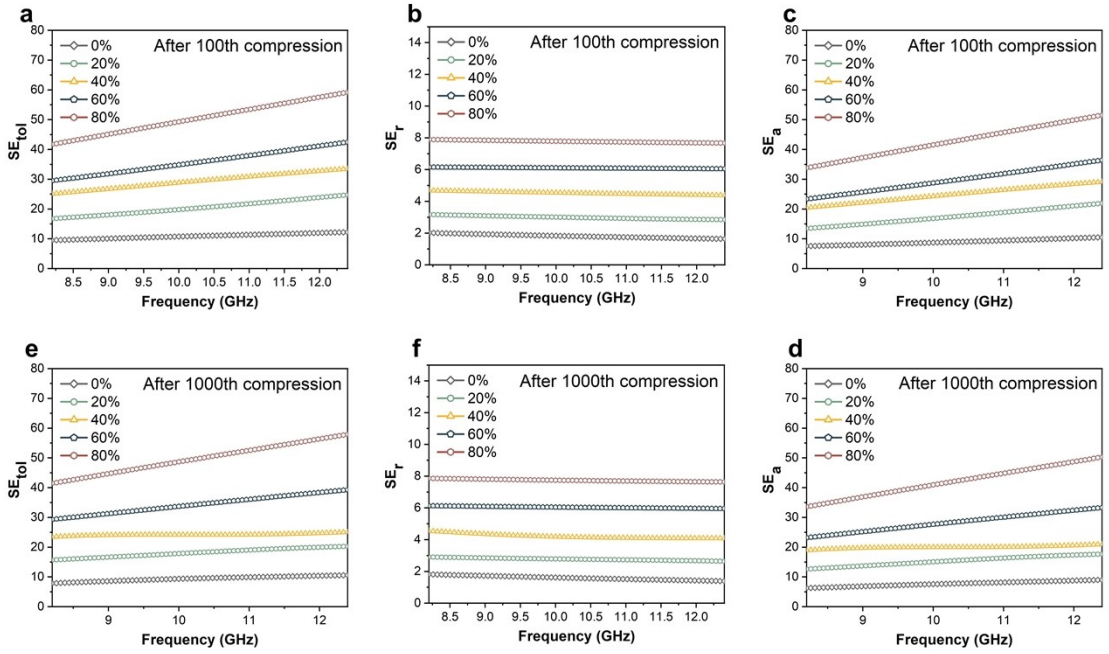


**Fig. S17** The $SE_{tol}$, $SE_r$, and $SE_a$ of the aerogel under 0%, 20%, 40%, 60%, and 80% strains before and after 100/1000 compression cycles.

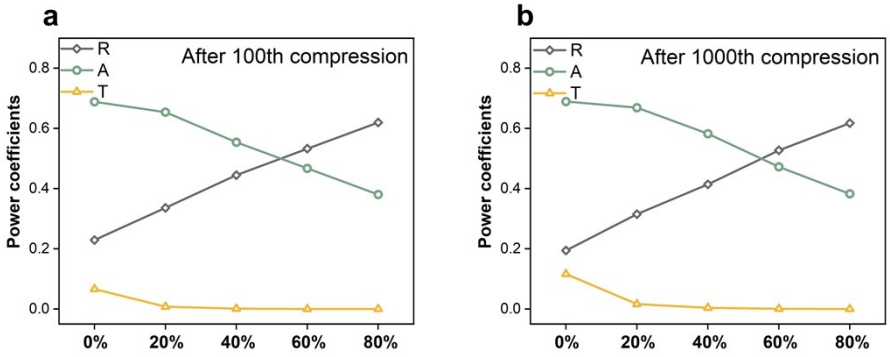


**Fig. S18** The R, A, and T values of the aerogel under 0%, 20%, 40%, 60%, and 80% strains before and after 100 and 1000 compression cycles.

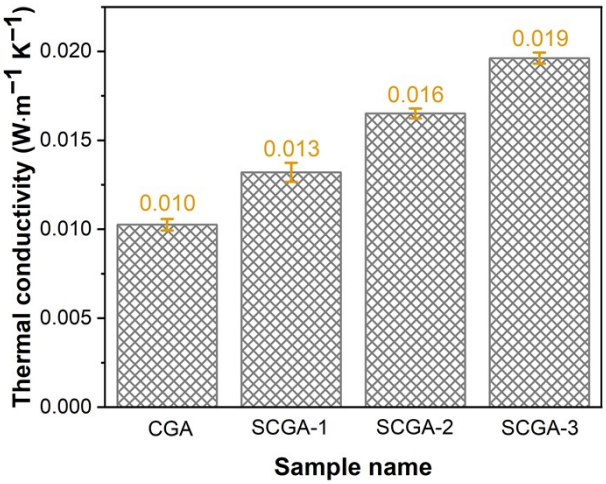


**Fig. S19** The thermal conductivity of CGA and SCGAs.

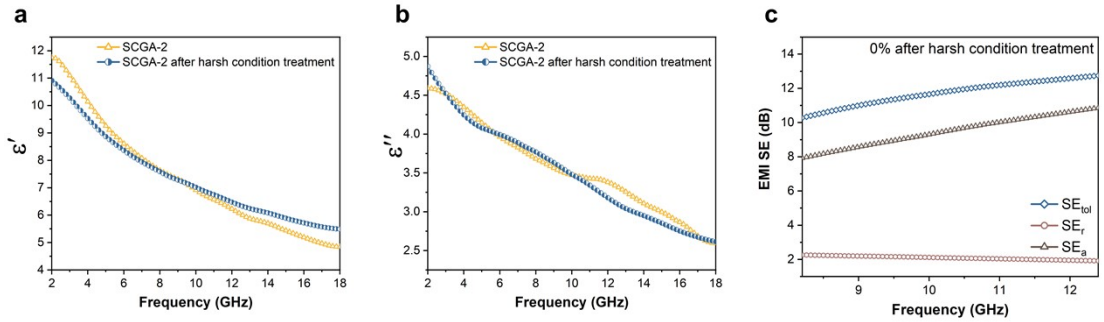


**Fig. S20** (a) ε′ and (b) ε″, for SCGA-2 before and after harsh condition treatments. (c) SE values under 0% strain for the SCGA-2 after harsh condition treatment.

**Table S1**. EAB comparison of SCGAs with the reported graphene/carbon-based aerogels

| Attenuators | $RL_{min}$/dB | d/mm | $EAB_{10}$/GHz | d/mm | REF |
|---|---|---|---|---|---|
| **Co@C/CG aerogel** | −45.02 | 1.5 | 4.02 | 1.5 | Small 2021, 17, 2102032 [1] |
| **PAN/CNT/$Fe_3O_4$ aerogel** | −59.85 | 1.5 | 2.8 | 1.5 | Adv. Funct. Mater. 2019, 29, 1807624 [2] |
| **N-rGA/Ni (500) aerogel** | −28.1 | 2.4 | 6.6 | 2.4 | Carbon 2019, 152, 575-586 [3] |
| **N-doped rGO aerogel** | −69.42 | 3.1 | 7.36 | 3.1 | Chem. Eng. J. 2022, 443, 136475[4] |
| **Carbon aerogel** | − 29.50 | 1.7 | 5.8 | 1.7 | Nano-Micro Lett. 2021, 13(1) [5] |
| **$MoS_2$/MXene aerogel** | −61.65 | 4.53 | 5.9 | 2 | Adv. Sci. 2022, 9, 2101988 [6] |
| **SiCnws@$SiO_2$-carbon foam** | −55.8 | 4.35 | 3.97 | 3.71 | Carbon 202 (2023) 103–111 [7] |
| **graphene@SiC aerogel** | -47.3 | 3 | 4.7 | 3 | Chem. Eng. J. 2018, 3337, 139376 [8] |
| **PANI/graphene aerogel** | −42.3 | 3 | 3.2 | 3 | Compos. B. Eng. 169 (2019) 221–228 [9] |
| **Defective graphene aerogel** | –43.11 | 5 | 6.4 | 2.65 | J. Colloid Interface Sci. 640 (2023) 680–687 [10] |
| **1T-$WS_2$/ CNT-rGO aerogel** | –56.63 | 1.15 | 3.84 | 1.2 | J. Mater. Chem. A, 2022,10, 13848-13857 [11] |
| **Ceramic-Confined Graphene Aerogel (SiCN/graphene)** | −57.9 | 1.7 | 5.0 | 1.7 | ACS Appl. Mater. Interfaces, 2023, 15 (33), 39559-39569 [12] |
| **SCGA-2** | -51.6 | 2.05 | 7.62 | 2.45 | This Work |

**Table S2**. Radar chart for the overall appreciation of the SCGAs compared with smart microwave compatible aerogel/foams.

| | **Smart MA aerogel[13]** | **Intelligent MA rGO/$VO_2$ Aerogel[14]** | **MA/transmission-switchable carbon aerogel [15]** | **MA/MS compatible (PEDOT:PSS) foam[16]** | **MS adjustable graphene foam [17]** | **This work** |
|---|---|---|---|---|---|---|
| **Dynamic MA/MS tailorability** | Off/on switchable smart MS (single function, strain stimuli) (6/10) | Off/on switchable MA (single function, temperature stimuli) (6/10) | MA/transmission-switchable (dual function, strain stimuli) (8/10) | MA/MS compatible (dual function, no stimuli) (5/10) | Adjustable MS (single function, strain stimuli) (6/10) | Dynamic tailorable MA/MS (dual function, strain stimuli) (9/10) |
| **Long-term mechanical reliably** | Stress retention of almost 100% after 30 cycles. Excellence resilience after 75 % compression strain. (8/10) | NA. (1/10) | Stress retention of almost 70% after 60,000 cycles; Excellence resilience after 80 % compression strain. (9/10) | Energy loss coefficient values from 19.25% to 16.17% after 200 cycles. (6/10) | Performance stable after 50 compression cycles (6/10) | Stress retention of 80% after 1000 cycles. Excellence resilience after 80% compression strain (8/10) |
| **Optimal MA/MS performance** | MS: $SE_{tol}$ of 27.6dB (5/10) | MA: EAB of 7.27 GHz $RL_{min}$ of -49 dB (6/10) | MA: $RL_{min}$ of 40 dB; Transmission: loss tangent < 0.4 (7/10). | MA: EAB of 10.52 GHz $RL_{min}$ of -57.57 dB MS: 30.8 dB (8/10) | MS: $SE_{tol}$ of 24.7 dB (5/10) | MA: EAB of 7.62 GHz $RL_{min}$ of -51.6 dB MS: $SE_{tol}$ of 50.1 dB (8/10) |
| **Harsh environment tolerance** | NA. (1/10) | NA. (1/10) | NA. (1/10) | Thermal insulation (5/10) | NA. (1/10) | Thermal insulation, fire resistance, anti-frosting, and tolerance to extremely low temperatures (10/10) |

**References**


1. J. Xu, X. Zhang, Z. B. Zhao, H. Hu, B. Li, C. L. Zhu, X. T. Zhang and Y. J. Chen, *Small*, 2021, **17**, 2102032.
2. Y. Li, X. F. Liu, X. Y. Nie, W. W. Yang, Y. D. Wang, R. H. Yu and J. L. Shui, *Adv. Funct. Mater.*, 2019, **29**, 1807624.
3. J. Tang, N. Liang, L. Wang, J. Li, G. Tian, D. Zhang, S. Feng and H. Yue, *Carbon*, 2019, **152**, 575-586.
4. J. Qiu, J. Liao, G. Wang, R. Du, N. Tsidaeva and W. Wang, *Chem. Eng. J.*, 2022, **443**, 136475.
5. W. H. Gu, J. Q. Sheng, Q. Q. Huang, G. H. Wang, J. B. Chen and G. B. Ji, *Nanomicro Lett.*, 2021, **13**, 1-14.
6. J. J. Yang, J. Q. Wang, H. Q. Li, Z. Wu, Y. Q. Xing, Y. F. Chen and L. Liu, *Adv. Sci.*, 2022, **9**, 2101988.
7. W. Deng, T. Li, H. Li, R. Niu, A. Dang, Y. Cheng and H. Wu, *Carbon*, 2023, **202**, 103-111.
8. Y. Jiang, Y. Chen, Y.-J. Liu and G.-X. Sui, *Chem. Eng. J*, 2018, **337**, 522-531.
9. Y. Wang, X. Gao, Y. Fu, X. Wu, Q. Wang, W. Zhang and C. Luo, *Compos. B. Eng.*, 2019, **169**, 221-228.
10. W. Yu and G. Shao, *J. Colloid Interface Sci.*, 2023, **640**, 680-687.
11. J. Zhou, J. Luo, G. Hao, F. Guo, G. Liu, H. Guo, G. Zhang, L. Xiao, Y. Hu and W. Jiang, *J. Mater. Chem. A*, 2022, **10**, 13848-13857.
12. G. Yu, G. Shao, Y. Chen and X. Huang, *ACS Appl. Mater. Interfaces*, 2023, **15**, 39559-39569.
13. X. Liu, Y. Li, X. Sun, W. Tang, G. Deng, Y. Liu, Z. Song, Y. Yu, R. Yu, L. Dai and J. Shui, *Matter*, 2021, **4**, 1735-1747.
14. Y. Zhao, H. Qi, X. Dong, Y. Yang and W. Zhai, *ACS Nano*, 2023, **17**, 15615-15628.
15. X. Li, L. Zhu, T. Kasuga, M. Nogi and H. Koga, *Chem. Eng. J.*, 2023, **469**, 144010.

16. W. Gu, S. J. H. Ong, Y. Shen, W. Guo, Y. Fang, G. Ji and Z. J. Xu, *Adv. Sci.*, 2022, **9**, 2204165.

17. B. Shen, Y. Li, W. Zhai and W. Zheng, *ACS Appl. Mater. Interfaces*, 2016, **8**, 8050-8057.